Nano Research
2022, 15(7): 6192–6199

ISSN 1998-0124 CN 11-5974/O4
https://doi.org/10.1007/s12274-022-4281-y

Synchronous constructing ion channels and confined space of Co_3O_4 anode for high-performance lithium-ion batteries

Yan Zhou[1], Chao Wang[1], Feiran Chen[1], Tingjuan Wang[1], Yaoyao Ni[1], Hongxia Sun[1], Nan Yu[1], and Baoyou Geng[1,2] (✉)

[1] *College of Chemistry and Materials Science, The Key Laboratory of Electrochemical Clean Energy of Anhui Higher Education Institutes, Anhui Provincial Engineering Laboratory for New-Energy Vehicle Battery Energy-Storage Materials, Anhui Normal University, Wuhu 241002, China*
[2] *Institute of Energy, Hefei Comprehensive National Science Center, Hefei 230031, China*

Received: 27 January 2022 / **Revised:** 23 February 2022 / **Accepted:** 28 February 2022

ABSTRACT

The yolk–shell structure has a unique advantage in lithium-ion batteries applications due to its ability to effectively buffer the volume expansion of the lithiation/delithiation process. However, its development is limited by the low contact point between the core and shell. Herein, we propose a general strategy of simultaneous construction of sufficient reserved space and multi-continuous active channels by pyrolysis of two carbon substrates. A double-shell structure consisting of Co_3O_4 anchored to hollow carbon sphere and external self-supporting zeolitic imidazolate framework (ZIF) layer was constructed by spray pyrolysis and additional carbon coating *in-situ* growth. In the process of high-temperature calcination, the carbon and nitrogen layers between the shells separate, creating additional space, while the Co_3O_4 particles between the shells remain are still in close contact to form continuous and fast electron conduction channels, which can realize better charge transfer. Due to the synergy of these design principles, the material has ultra-high initial discharge capacities of 2,183.1 $mAh\cdot g^{-1}$ at 0.2 $A\cdot g^{-1}$ with capacity of 1,121.36 $mAh\cdot g^{-1}$ after 250 cycles, the long-term capacities retention rate is about 92.4% after 700 cycles at 1 $A\cdot g^{-1}$. This unique channel-type double-shell structure fights a way out to prepare novel electrode materials with high performance.

KEYWORDS

double-shell structure, ion channels, confined space, lithium-ion batteries, Co_3O_4

1 Introduction

Lithium-ion batteries (LIBs) have been widely used in electronic fields due to their ability to provide higher mass and volume energy density [1, 2]. However, the relatively low theoretical capacities of conventional graphite anodes limit the commercial application of LIBs [3–5]. Fortunately, niobium-based oxides ($Nb_{12}O_{29}$, $MoNb_{12}O_{33}$, $V_3Nb_{17}O_5$, $TiNb_2O_7$, $Al_{0.2}Fe_{0.8}Nb_{11}O_{29}$, etc.), vanadium-based oxides ($Na_2Ca(VO_3)_4$, VPO_5, etc.), and metal oxides such as Co_3O_4 have excellent physical and electrochemical properties, which can meet the requirements of high-performance LIBs. However, due to the inherent low conductivity of metal oxides (MOs) and the volume collapse caused by the lithium–delithiation process, electrode pulverization and agglomeration can be induced, resulting in a rapid decrease in circulating capacity [6–9]. Structural regulation, especially the construction of cavity structure, has become an important strategy to improve lithium capacity [10–13]. For example, Guo et al. fixed Co^{2+} in alginate fiber through a typical "egg-box" and changed the adsorption depth of Co^{2+} to achieve ion gradient distribution by adjusting the ratio of mixed water/ethanol solvent [10]. Multi-shell hollow Co_3O_4 fibers showed the best performance (940.2 $mAh\cdot g^{-1}$ after 200 cycles at 1 $A\cdot g^{-1}$). However, the structural regulation on the improvement of electronic conductivity is minimal, so the combination of high conductivity carbon materials and metal MOs becomes an effective means to improve the conductivity [14–16]. For example, Geng et al. prepared Co_3O_4-doped hollow porous carbon microspheres by spray pyrolysis to control the carbon content in the microspheres by adjusting the ratio of Co^{2+} to glucose [17]. Although cavity structures can provide additional storage space for lithium ions, lithium ion transport processes often lack efficient channels [18–22]. The uniform and effective contact between MOs and conductive carrier also restricts the lithium storage performance. Therefore, it is equally important to construct ion transport channels and extra lithium storage cavity for metal oxide electrode materials.

Herein, we report a strategy of simultaneous pyrolysis of two carbon substrates to create a functional reserved space between double carbon–nitrogen shells and an interdiffusion active Li^+ channel for carbon–Co_3O_4–carbon. Firstly, Co_3O_4/C hollow spheres were prepared by spray pyrolysis method [23, 24], and then Co_3O_4 was dissolved on the surface of hollow spheres by dimethylimidazole to form Co^{2+}, which diffuses outward and coordinates with dimethylimidazole to grow continuously, forming the supported zeolitic imidazolate framework (ZIF) layer. Finally, during the high-temperature calcination process, a few of amorphous carbon in the inner shell still maintain a stable microsphere structure, while a large number of highly crystalline carbon layers in the outer shell shrink to produce extra space, which contributes to the capacity and effectively restrict the

Address correspondence to bygeng@mail.ahnu.edu.cn

formation of structural collapse and cracks. Meanwhile, the Co_3O_4 particles in the inner shell are oriented to grow and arrange in close contact with the Co_3O_4 pillar of the shell, forming a continuous and rapid Li^+ channel and a conductive matrix with high strength, which has a lower surface-interface electron/ion diffusion resistance and achieves better charge transfer. The design fully grasps the balance between the volume effect of the composite and the effective ion channel construction. The performance testing shows that the prepared double-shell Co_3O_4 composite capacities are 1,121.36 $mAh \cdot g^{-1}$ after 250 cycles at 0.2 $A \cdot g^{-1}$ and the long-term capacities retention rate is 92.4% after 700 cycles at 1 $A \cdot g^{-1}$.

2 Experimental section

2.1 Materials

All chemical reagents were purchased from commercial sources and used without any further purification: $Co(NO_3)_2 \cdot 6H_2O$(AR), N-methyl-2-pyrrolidone (NMP), and 2-methylimidazole (98%) were got by Aladdin Industrial Corporation. Polyvinylidenefluoride (PVDF), Cu foil (10 mm thickness), metallic Li (0.6 mm thickness, 99.9%), a separator (Celgard 2325), and Super-P-Li (carbon black) were got by Lizhiyuan Battery Materials Company. The above chemicals were not further purified.

Synthesis of Co_3O_4@C. The molar ratios of $Co(NO_3)_2 \cdot 6H_2O$ (AR) and polyvinyl pyrrolidone (PVP) in deionized water (40.0 mL) were 8:0, 8:2, and 8:4, respectively. The concentration of cobalt ion in the solution was 0.5 mol/L and stirred for 30 min. The aerogel formed from the mixed solution was then decomposed in a spray pyrolysis apparatus at 500 °C, and the resulting sample was dried at 60 °C for 12 h. Finally, the dried powder was calcined in Ar atmosphere at 500 °C for 4 h to obtain the black product. The corresponding samples were Co_3O_4, S8-2, and S8-4.

Synthesis of Co_3O_4 CN double-shell. First, 0.1 g of the spray pyrolysis product of step 1 (8:2) was dissolved in 10.0 mL deionized (DI) water and 10.0 mL ethanol with stirred evenly. Second, 1.0 g of 2-methylimidazole (98%) was added in above mixed solution. After ultrasonic treatment for 30 min, uniform mixed solution was obtained. Stirring at room temperature for 3 h. After the reaction, the samples were centrifuged with water and ethanol for 3 times, and placed in a vacuum drying oven for 12 h. Finally, the dry powders were calcined at 500 °C for 4 h in an Ar atmosphere to obtain Co_3O_4@NC double-shell microspheres.

2.2 Material characterization

The crystalline phase of products was tested by X-ray diffraction (XRD) with Cu Kα radiation (Bruker AXS, D8 Advance). Element valence states on the surface of composite materials were analyzed with X-ray photoelectron spectroscopy (XPS) with Al Kα X-ray radiation (Thermo Fisher, ESCALAB 250XI). By high resolution transmission electron microscopy (HRTEM, FEI Tecnai G220), transmission electron microscopy (TEM, Hitachi HT-7700), and field emission scanning electron microscopy (FESEM, Hitachi S-8100), we can observe the structure, size, and morphology of the samples. We can analyze samples pore size distribution and specific surface area by automated gas sorption analyzer (Micromeritics, ASAP2010N). The thermogravi-metric analysis (TGA) was performed on thermogravimetric analyzer (TA, Q500) under air.

2.3 Electrochemical measurements

The mixed slurry was made of the product obtained from the experiment, Super-P-Li, and PVDF in a weight ratio of 7:2:1. And it was coated onto clean Cu foil, and dried for 24 h. The working electrode was assembled into a 2,032 coin cells in a glove box, and the mass loading of working electrode's active material was 1.1–1.4 $mg \cdot cm^{-2}$. 1 M $LiPF_6$ added in the mixed ethylene carbonate/dimethyl carbonate (EC/DEC) (volume ratio = 1:1) was used as the electrolyte solution. Battery performance was tested on a battery test system (Neware, CT-4008) at 25 °C. The cyclic voltammetry (CV) was tested on an electrochemical workstation (Chenhua, CHI660C) at a scan rate of 0.2 $mV \cdot s^{-1}$. In addition, the electrochemical impedance spectroscopy (EIS) plots were tested at 10 mV of amplitude and in a frequency range from 0.1 MHz to 0.01 Hz.

3 Results and discussion

The fabrication process of Co_3O_4@CN double-shell microspheres can be illustrated by Scheme 1. To begin with, a certain proportion of cobalt nitrate and PVP were used as raw materials to synthesize Co_3O_4 hollow spheres by spray pyrolysis. Next, dimethylimidazole reacted with hollow spheres to dissolve Co_3O_4 into Co^{2+}, and Co^{2+} diffused outward to realize continuous growth and form Co_3O_4@ZIF. Finally, Co_3O_4@CN double-shell microspheres were obtained by high-temperature calcination. The two-dimensional (2D) section view more clearly illustrates the growth mechanism

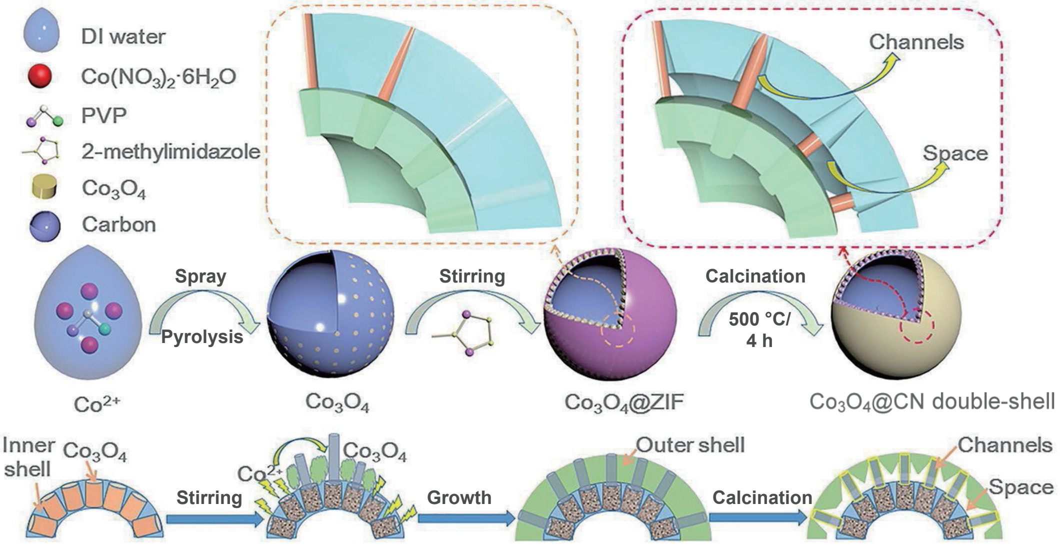

Scheme 1 Schematic representation of Co_3O_4@CN double-shell microspheres composites.

of double-shell microspheres and the synchronous customization of interface channels and confined space. We believe that this unique structure is of great significance for constructing high-performance lithium-ion batteries.

As expected, Co_3O_4@CN double-shell microspheres have been formed as shown in Fig. 1(a) which observed in SEM images. Figure 1(b) shows a microsphere with a diameter of about 700 nm, which clearly demonstrates the characteristics of the double-shell structure. Figure 1(c) further reflects the microstructure between the double-shell. It is worth noting that there is not a single cavity structure between the interfaces of the double-shell, but there is a cross-shaped strut in which a cross-interleaved zigzag is present, as shown in the inseted diagram. The formation of double-shell microspheres is due to dimethylimidazole can cross the pores of ZIF, react with Co_3O_4 in the inner shell, and deprotonate with the generated H^+, so that a small amount of Co_3O_4 is dissolved in Co^{2+}. On the outer surface of the ZIF layer, Co^{2+} diffused outwards and reacted with a large number of ligands to achieve continuous growth. The synchronous formation of channel and space is attributed to the difference of Co_3O_4 and carbon content between the double-shell (depending on the proportion of the Experimental section). The inner shell is a hollow sphere composed of quite a little of Co_3O_4 particles and little of amorphous carbon, and an outer shell is little of Co_3O_4 particles and a pretty little of highly crystalline carbon layers. During the calcination process, the Co_3O_4 pillars of an outer shell, grown and arranged directionally with Co_3O_4 particles in the inner shell as a self-sacrificing template, did not change, thus constituting interface channels. On the other hand, the carbon matrix produces inherent decomposition at high temperatures, so the decomposition of a large amount of carbon in the shell generates part of the space. Meanwhile, the self-supporting effect of the Co_3O_4 pillar in the shell inhibits the shrinkage of part of the highly crystalline carbon layer to generate additional space. In addition, Fig. S1 in the Electronic Supplementary Material (ESM) shows that the double-shell were closely connected before calcination, and additional space was generated between the double-shell after high-temperature calcination. TEM images at different magnification further directly prove the existence of Co_3O_4 channels connected (Fig. 1(g)) and the formation of space between the double-shell (Fig. 1(k) and Fig. S2 in the ESM). HRTEM (Fig. 1(d)) shows that the lattice spacing of Co_3O_4 in the ZIF layer is 0.202 nm, which is consistent with the lattice fringe of the inner shell edge. Figure 1(h) shows that the lattice spacing of Co_3O_4 in the inner shell is 0.46 nm. This is consistent with the growth mechanism of Co_3O_4@CN double-shell. TEM images (Figs. 1(e), 1(f), and 1(i)) confirmed that the inner shell maintained a stable microsphere structure during the calcination process, while the outer shell shrank from creating space, and there were good interface channels between the double-

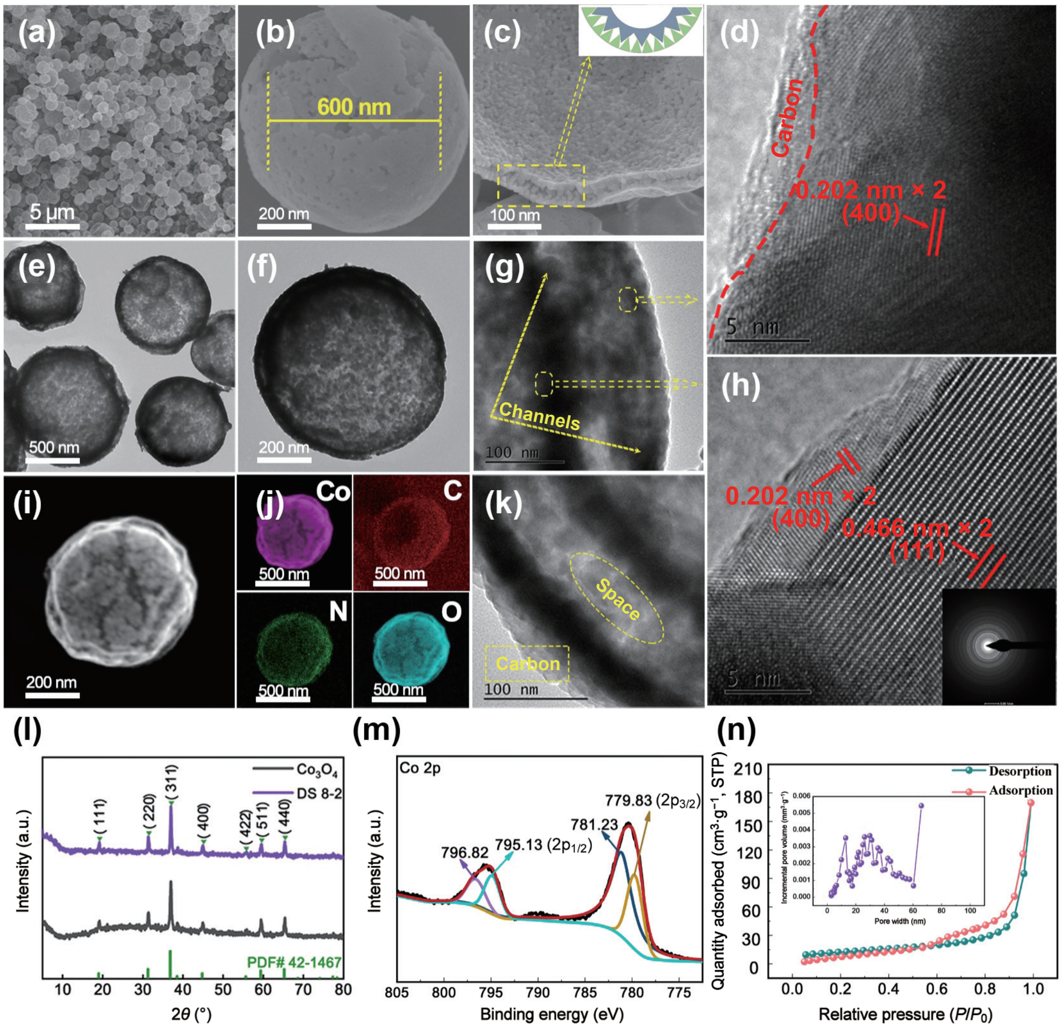

Figure 1 (a)–(c) SEM images of Co_3O_4@CN double-shell. TEM images (e)–(g) and (k) of Co_3O_4@CN double-shell. (d) and (h) HRTEM images of the double-shell, respectively. (i) and (j) The scanning TEM (STEM) image and the corresponding elemental mapping images of the product. (l) XRD patterns of the Co_3O_4 and Co_3O_4@CN double-shell. (m) XPS spectra of Co 2p for the Co_3O_4@CN double-shell. (n) N_2 adsorption/desorption isotherm and Barrett–Joyner–Halenda (BJH) pore size distribution curves of Co_3O_4@CN double-shell.

shell. Transmission element mappings of product as shown in Fig. 1(j), and the uniform distribution of C, N, Co, and O can be observed, which is also proved by energy-dispersive X-ray (EDX) result in Fig. S3 in the ESM.

In this case, the hollow sphere, crumpled sphere, and Co_3O_4@CN double-shell sphere are named S8-2, S8-4, and double-shell 8-2 (DS 8-2), respectively, according to the proportion of Co^{2+} and PVP. Figures S4–S6 in the ESM show SEM and TEM images of Co_3O_4, S8-2, and S8-4. Figure S4 in the ESM was prepared without PVP template, from which we can see that the material shows a solid spherical structure, and the voids on the surface are related to the rapid evaporation of solvent during the reaction process. With the increase of PVP, the morphology gradually changed from solid sphere to hollow sphere (Fig. S5 in the ESM) and then to crumpled sphere (Fig. S6 in the ESM). During spray pyrolysis, the content of PVP will affect the surface tension of the solvent, which is the key to regulating the pore morphology, similar to the principle of blowing balloons. It can be seen that the change of morphology is due to the change of PVP concentration in critical micelle concentration, which inhibits balloon expansion in the pyrolysis process.

The phase and crystal structure of the product can be determined by XRD analysis. The diffraction peaks of samples Co_3O_4, double-shell 8-2 (Fig. 1(l)) and S8-2 (Fig. S7(a) in the ESM) were in good consistent with cubic Co_3O_4 (JCPDS #42-1467) [25]. No other characteristic peaks were found, indicating that the samples had good crystallinity and purity. However, it is worth noting that S8-4 (Fig. S7(b) in the ESM) is not calcined adequately because it contains more carbon and generates partial cubic CoO (JCPDS #48-1719) [26]. To further analyze the elemental analysis of the sample surface, we carried out XPS measurement [27–30]. The XPS spectra showed the presence of Co, O, C, and N elements in the samples. Figure 1(m) is a high-resolution XPS spectra of the product. We can observe that the Co 2p is decomposed into two characteristic peaks of 779.8 and 795.1 eV, which is consistent with Co $2p_{3/2}$ and Co $2p_{1/2}$. In addition, the cubic Co_3O_4 definite rule is attributed to the binding energy difference and peak strength ratio of the two characteristic peaks. Figure S8(a) in the ESM is the XPS survey spectrum. Figure S8(b) in the ESM is the XPS spectra of C 1s. The characteristic peak of 284.83 eV corresponds to C=C/C–C peak, and 286.85 eV corresponds to O–C=O. Figure S8(c) in the ESM in the XPS spectra of N 1s can be de-discovered into three peaks: 398.93, 399.53, and 406.23 eV, corresponding to the pyridinic N, pyrrolic N, and graphitic N. The presence of Co_3O_4 was further confirmed by the O 1s spectra at 529.83 eV (Fig. S8(d) in the ESM). In addition, the specific surface area and pore structure of Co_3O_4, S8-2, S8-4, and double-shell 8-2 were determined by the nitrogen adsorption/desorption method [31–33]. It is not difficult to find that double-shell 8-2 has a specific surface area of 104.61 $m^2 \cdot g^{-1}$ (Fig. 1(n)), higher than S8-2 of 74.35 $m^2 \cdot g^{-1}$ in Fig. S9(b) in the ESM, which is caused by the space generated during pyrolysis. However, the specific surface area of hollow carbon spheres is much higher than that of solid spheres (32.27 $m^2 \cdot g^{-1}$ in Fig. S9(a) in the ESM) and crumpled spheres (13.85 $m^2 \cdot g^{-1}$, Fig. S9(c) in the ESM), indicating that the shape control of materials is also crucial to the specific surface area. Figure 1(n) shows that the pore size distribution is between 10–40 nm, indicating a typical microporous and mesoporous material. The double-shell can provide a higher specific surface area and even the aperture distribution, which is beneficial to the insertion and delamination of lithium-ion, alleviates volume expansion, and improves electrolyte immersion and sample cycle stability.

CV electrochemical characterization indicated the properties of the product. The first three cyclic voltammetry curves are shown in Fig. 2(a). Co_3O_4 only has a substantial reduction peak near 0.784 V in the first discharge [34–36], which is due to the reduction of metal Co and the formation of solid electrolyte interface (SEI) film in the process of $Co_3O_4 + 8Li^+ + 8e^- \rightarrow 3Co + 4Li_2O$. Due to the oxidation of Co to CoO ($Co + Li_2O \rightarrow CoO + 2Li^+ + 2e^-$), a prominent oxidation peak appears at 2.032 V and the weak peak at 2.773 V is due to the decrease of electrolyte. In the second and third stages, the substantial reduction peak was replaced by two broad peaks, which split into 0.762 and 0.754 V, and the intensity decreased significantly in the subsequent cycle, indicating that a multi-step reaction occurred during the discharge process. Some irreversible transformation and structural modification took place in the first cycle [37]. The oxidation peak was located near 2.014 V. During the subsequent cycle, the intensities of the reduction peaks and oxidation peaks are substantially consistent, indicating that double-shell 8-2 microspheres as anode materials have impressive cycling stability. The charge–discharge curves of double-shell 8-2 and Co_3O_4 in the first three cycles at 0.2 $A \cdot g^{-1}$ are shown in Fig. 2(b). The initial discharge capacities and charge capacities are 2,183.1 and 1,666.22 $mAh \cdot g^{-1}$, which are much higher than the theoretical capacities of carbon (372 $mAh \cdot g^{-1}$) and even Co_3O_4 (890 $mAh \cdot g^{-1}$) and equivalent to 76.3% of the initial coulombic efficiency. The specific discharge capacities of the second and third cycles are 1,647.88 and 1,491.47 $mAh \cdot g^{-1}$ and the capacities retention rates are 88.8% and 90.6%. The initial discharge capacities and charge capacities of Co_3O_4 (Fig. S10 in the ESM) are 1,110.11 and 748.53 $mAh \cdot g^{-1}$. The specific discharge capacities of the second and third cycles are 757.09 and 474.63 $mAh \cdot g^{-1}$ and the Coulombic efficiency are 61.8% and 78.6%. It was evident that the structure and composition of Co_3O_4 can affect the charging and discharging process during the cycle [38, 39]. During the subsequent cycle, the Coulombic efficiency of double-shell 8-2 sample remained 100%.

The rate performance of double-shell 8-2 is shown in Fig. 2(c). At the current density of 0.2, 0.5, 1.0, 2.0, and 5.0 $A \cdot g^{-1}$, the average charge capacities are 1,124.57, 713.22, 683.05, 493.67, and 389.58 $mAh \cdot g^{-1}$, respectively. When the sample after 50 cycles at 0.2 $A \cdot g^{-1}$ again, the charging capacities reache 1,168.71 $mAh \cdot g^{-1}$, which verifies the double-shell 8-2 has excellent cycling stability, and the material prepared by this method has good performance of lithium-ion batteries. As shown in Fig. 2(d), after 150 cycles, the specific discharge capacity remains at 1,408.01 $mAh \cdot g^{-1}$ and after 250 cycles, it remains at 1,121.36 $mAh \cdot g^{-1}$. The charge–discharge capacities tend to be stable, and the Coulomb efficiency is more than 99%. More specifically, the key to long-term cyclic stability is the continuous formation of SEI films on new surfaces due to volume changes, which may affect lithium storage, leading to capacity decline at an early stage. However, in the subsequent charge–discharge cycle, Co_3O_4@CN double-shell SEI films tend to stabilize immediately, indicating that the spatial structure between double-shells induced by ZIF effectively limits the structure collapse and crack. At the same time, the excellent conductivity is attributed to the existence of multiple continuous and fast Li^+ channels between the double shells, forming more Li^+ sites and strength conductive matrix. Figure 2(f) shows that double-shell 8-2 still retains 798.247 $mAh \cdot g^{-1}$ specific discharge capacities after 200 cycles and 667.41 $mAh \cdot g^{-1}$ specific discharge capacities after 700 cycles under the current density of 1 $A \cdot g^{-1}$. However, the performance of Co_3O_4, S8-2, and S8-4 samples is poor. Figure S11(a) in the ESM shows that during the first 150 cycles, the capacities of Co_3O_4, S8-2, and S8-4 are 539.23, 924.86, and 841.56 $mAh \cdot g^{-1}$, respectively. Figure S11(b) in the ESM shows that the specific discharge capacities of Co_3O_4, S8-2, and S8-4 samples are 189.39, 405.9, and 354.38 $mAh \cdot g^{-1}$, respectively. Figure 2(e) and

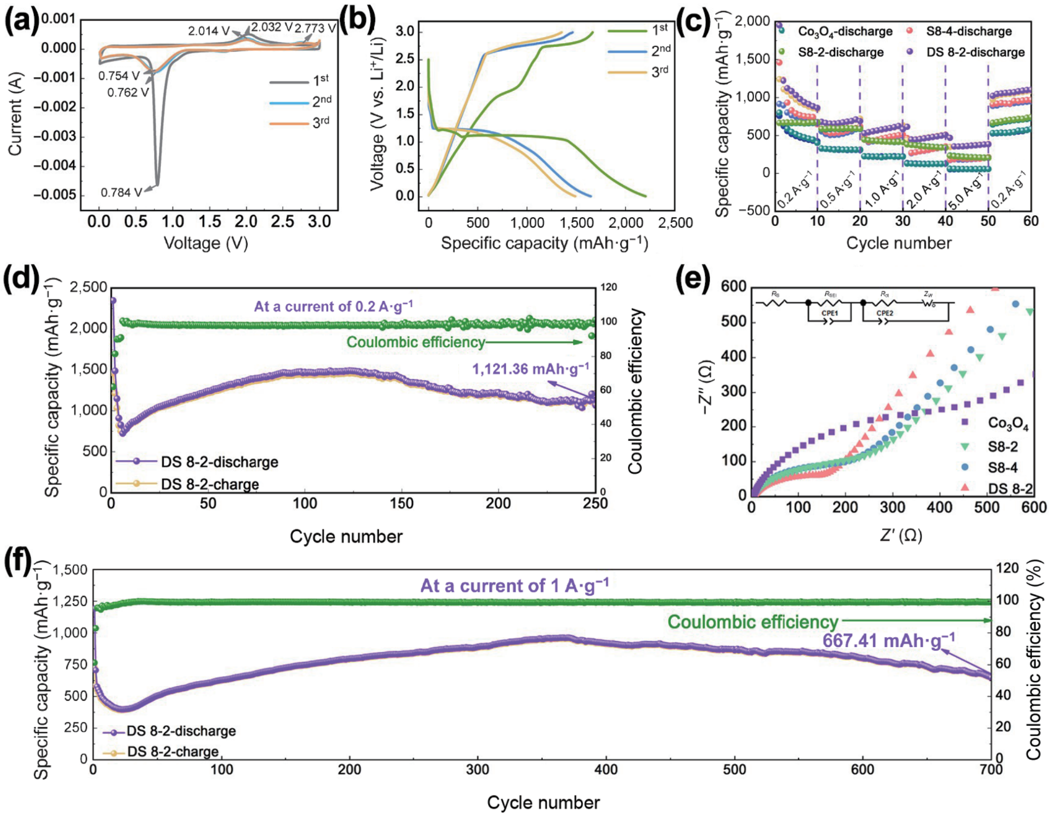

Figure 2 (a) CV curves of double-shell 8-2 as anode materials at a scan rate of 0.2 mV·s^{-1} between 0.01 and 3.0 V versus Li/Li$^+$, (b) charge–discharge curves of the first three cycles of the product, and (c) rate performance of them at various current densities from 0.2 to 5.0 A·g^{-1}. (d) Cyclic performance of double-shell 8-2 at the current density of 0.2 A·g^{-1} after 250 cycles. (e) EIS of double-shell 8-2 after 20 cycles at a rate of 1 A·g^{-1}, and the inset shows the equivalent circuit. (f) Cyclic performance of double-shell 8-2 at the current density of 1 A·g^{-1} after 700 cycles.

Fig. S12 in the ESM show the electrochemical impedance spectra of double-shell 8-2 electrode material after 20 cycles at 1 A·g^{-1} cycle rate. The semicircle and straight line on the curve reflect the insertion transfer resistance and diffusion of lithium ions in the electrode, respectively. The galvanostatic intermittent titration technique (GITT) profiles showed that the construction of channels can effectively guide the lithiation/delithiation process and accelerate the reaction kinetics (Fig. S13 in the ESM) [40]. In contrast, double-shell 8-2 has the best transmission performance, mainly due to the construction of the interface channel and the presence of double carbon–nitrogen shell. Specifically, its impedance value of 150.3ω is much smaller than that of Co$_3$O$_4$, S8-2, and S8-4 samples, consistent with GITT tests. In Table S1 in the ESM, the prepared material has ultra-high lithium storage properties compared to some similar studies.

Pseudocapacitance behavior is a Faraday process that occurs on the surface of electrode materials and involves the characteristics of rapid charge and discharge of materials. Its existence is conducive to improving lithium-ion transport capacity [41–43]. Figure S14 in the ESM provides an in-depth study of the pseudocapacitance contribution of the prepared double-shell 8-2. As shown in Fig. S14(a) in the ESM, the CV curves of the material were tested at the scanning rates of 0.1, 0.3, 0.6, 0.9, and 1.2 mV·s^{-1} and the dynamics of double-shell 8-2 as anode materials was further studied. It is proved that the existence of channels between double carbon and nitrogen shells can improve the transport capacity of Li$^+$ to some extent. In addition, with the increase of scanning rate, the peak current variation trend of cathode and anode indicates that the reaction is a surface process. Assume that the peaks of current (I) and scan speed (v) obey a power–law relationship: $I = av^b$, where a and b are constants. The b value is related to the intrinsic kinetics of the electrode reaction and is determined by a curve between $\log I = b\log v + \log a$, generally between 0.5 and 1. b value equals to 0.5 and is the diffusion control process, while b value equals to 1 and is the surface capacitance control process [44, 45]. In Fig. S14(b) in the ESM, the b values of the oxidation peak and reduction peak are 0.644 and 0.608, indicating that double-shell 8-2 as anode materials have pseudocapacitance behavior in the reaction process. The total charge contribution can be quantified by separating the specific contribution of the capacitor process from the diffusion control charge at a given voltage, and can be calculated at a given scanning rate according to the following formula: $I\,(V) = k_1v + k_2v^{1/2}$, where k_1v is the capacitor control component and k_2v is the diffusion control component [46]. Figure S14(c) in the ESM shows the separation of the capacitor control component (shaded area) and the total charge when the scanning rate is 0.9 mV·s^{-1}. By calculation, the capacitor contribution accounts for 81.283% of the total value at the scanning speed of 0.9 mV·s^{-1}. The capacitor control component's contribution increases with the sweep speed increases, as shown in Fig. S14(d) in the ESM. When the sweep speed is 0.1, 0.3, 0.6, and 1.2 mV·s^{-1}, pseudocapacitance control components accounted for 68.037%, 72.894%, 77.572%, and 85.351%, respectively. The results show that the channels between carbon and nitrogen shell to a certain extent, improved its on the electrochemical performance of dynamic capabilities, which is mainly due to the carbon and nitrogen shell increase the contact area of material surface and the electrolyte, and special carbon–Co$_3$O$_4$–carbon channel shortened the Li$^+$ electrode internal transmission path. Therefore, the performance of lithium-ion batteries is improved to a certain extent.

Based on the performance differences between materials of Co$_3$O$_4$, S8-2, S8-4, and double-shell 8-2 in Fig. 3(a) by observing the electrode material after circulation, the Co$_3$O$_4$ solid sphere is wholly broken into small particles (Fig. S15 in the ESM); basically, the S8-2 hollow sphere is part of the spherical structure. However,

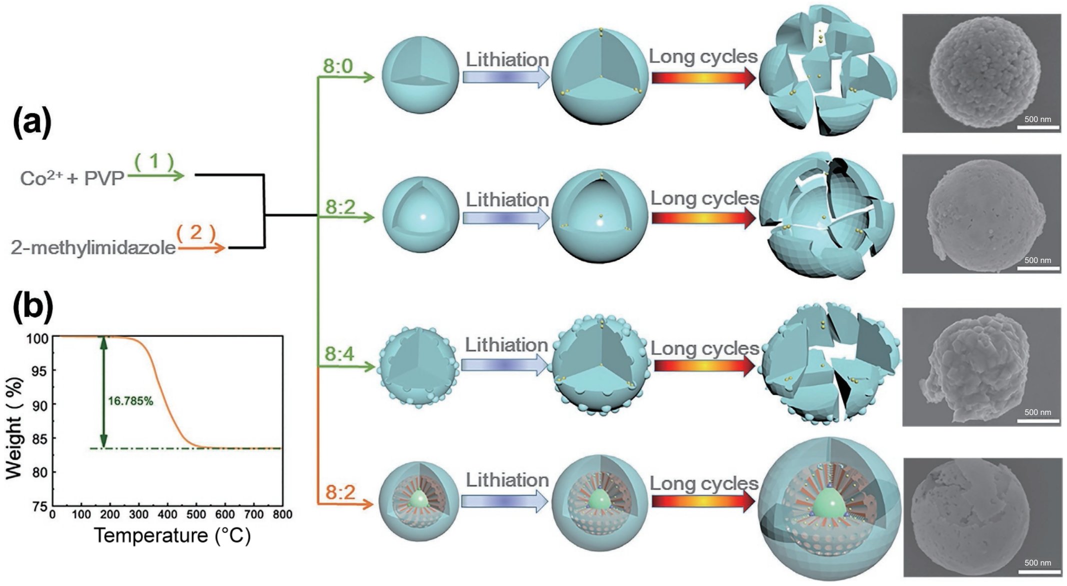

Figure 3 (a) Schematic illustration of the structure changes and transfer channels of ions and electrons during the cycling process. (b) The TG curve of double-shell 8-2.

the quantity is less (Fig. S16 in the ESM), the S8-4 shrivel sphere into a similar to the block structure (Fig. S17 in the ESM), it is essential to note that compared with S8-2, there are more spherical structures in the double-shell 8-2, and the morphology remains intact (Fig. S18 in the ESM), which may be the fundamental reason for the performance difference. Based on the above analysis, the following three strategically interdependent characteristics of double-shell 8-2 are responsible for their excellent anode performance. Firstly, the double carbon–nitrogen shell structure provides a better constraint for Co_3O_4 and dramatically alleviates the volume expansion effect. Figure 3(b) shows that the carbon content was 16.785% compared with that of Co_3O_4, and it was observed that the mass fraction of carbon was close to that in EDX result in Fig. S3 in the ESM. Secondly, the reserved space formed between the double-shell provides more storage sites. This is the key to constituting a high capacity. Finally, it is built multi-continuous active channels between the double-shell. It is a self-supporting effect in lithiation/delithiation process, but also promotes the efficient recovery of lithium-ions, thereby significantly improving electron conductivity and stability of the entire electrode.

4 Conclusion

In summary, we constructed Co_3O_4@CN double shell composite with specific reserved space and multiple continuous Li^+ active channels. Different carbon pyrolysis between the double shells generates additional lithium storage space. The self-supported ZIF layer based on the directional growth of the inner shell has a well-arranged hierarchical structure. The bonded together combination between the two guarantees fast Li^+ transfer between electrodes and ultra-high structural stability. Due to these design synergies, this composite material can provide excellent lithium storage properties. When the current density is 0.2 $A \cdot g^{-1}$, the specific capacity remains at 1,121.36 $mAh \cdot g^{-1}$ after 250 cycles. When the current density is 1 $A \cdot g^{-1}$, the long-term capacity retention rate is about 92.4% after 700 cycles. This unique channel double-shell structure provides a new design for preparing high-performance novel electrode materials.

Acknowledgements

This work was supported by the National Natural Science Foundation of China (Nos. 21871005 and 22171005), the Program for Innovative Research Team of Anhui Education Committee, the Project for Collaborative Innovation of Anhui Higher Education Institutes (Nos. GXXT-2020-005, GXXT-2021-012, and GXXT-2021-013), the Natural Science Foundation of the Education Department of Anhui Province (No. KJ2020A0075), and the Foundation of the Anhui Province Key Laboratory of Clean Energy Materials and Chemistry for Sustainable Conversion of Natural Resources (No. LCECSC-10).

Electronic Supplementary Material: Supplementary material (additional FESEM and TEM images, XRD patterns, Brunauer–Emmett–Teller (BET) surface area, EDX mappings, CV curves, cyclic performances, EIS spectra, charge/discharge curves, and table comparison of material) is available in the online version of this article at https://doi.org/10.1007/s12274-022-4281-y.

References

[1] Tarascon, J. M.; Armand, M. Issues and challenges facing rechargeable lithium batteries. *Nature* **2001**, *414*, 359–367.

[2] Choi, J. W.; Aurbach, D. Promise and reality of post-lithium-ion batteries with high energy densities. *Nat. Rev. Mater.* **2016**, *1*, 16013.

[3] Jiao, S. Q.; Fu, J. M.; Wu, M. Z.; Hua, T.; Hu, H. B. Ion sieve: Tailoring Zn^{2+} desolvation kinetics and flux toward dendrite-free metallic zinc anodes. *ACS Nano* **2022**, *16*, 1013–1024.

[4] Liu, W.; Liu, P. C.; Mitlin, D. Review of emerging concepts in SEI analysis and artificial SEI membranes for lithium, sodium, and potassium metal battery anodes. *Adv. Energy Mater.* **2020**, *10*, 2002297.

[5] Qin, K. Q.; Holguin, K.; Mohammadiroudbari, M.; Huang, J. H.; Kim, E. Y. S.; Hall, R.; Luo, C. Strategies in structure and electrolyte design for high-performance lithium metal batteries. *Adv. Funct. Mater.* **2021**, *31*, 2009694.

[6] Liu, H.; Liu, X.; Wang, S. L.; Liu, H. K.; Li, L. Transition metal based battery-type electrodes in hybrid supercapacitors: A review. *Energy Storage Mater.* **2020**, *28*, 122–145.

[7] Cong, L. D.; Zhang, S. C.; Zhu, H. Y.; Chen, W. X.; Huang, X. Y.; Xing, Y. L.; Xia, J.; Yang, P. H.; Lu, X. Structure-design and theoretical-calculation for ultrasmall Co_3O_4 anchored into ionic liquid modified graphene as anode of flexible lithium-ion batteries. *Nano Res.* **2022**, *15*, 2104–2111.

[8] Hou, J. B.; Yang, M.; Wang, D. Y.; Zhang, J. L. Fundamentals and challenges of lithium ion batteries at temperatures between-40 and 60 °C. *Adv. Energy Mater.* **2020**, *10*, 1904152.

[9] Wu, D. B.; Wang, C.; Wu, H. J.; Wang, S.; Wang, F. Q.; Chen, Z.; Zhao, T. B.; Zhang, Z. Y.; Zhang, L. Y.; Li, C. M. Synthesis of hollow Co_3O_4 nanocrystals *in situ* anchored on holey graphene for

high rate lithium-ion batteries. *Carbon* **2020**, *163*, 137–144.

[10] Dong, Y.; Jiang, X. Y.; Mo, J. H.; Zhou, Y. Z.; Zhou, J. P. Hollow CuO nanoparticles in carbon microspheres prepared from cellulose-cuprammonium solution as anode materials for Li-ion batteries. *Chem. Eng. J.* **2020**, *381*, 122614.

[11] Li, L.; Dai, J.; Jiang, G. X.; Sun, X. Y.; Huang, Z. H.; Xie, Z. J.; Cao, B. Q. Three-dimensional mesoporous straw-like Co_3O_4 anode with enhanced electrochemical performance for lithium-ion batteries. *ChemistrySelect* **2019**, *4*, 6879–6885.

[12] Wang, C. H.; Bai, G. L.; Yang, Y. F.; Liu, X. J.; Shao, H. X. Dendrite-free all-solid-state lithium batteries with lithium phosphorous oxynitride-modified lithium metal anode and composite solid electrolytes. *Nano Res.* **2019**, *12*, 217–223.

[13] Yan, C. S.; Chen, G.; Zhou, X.; Sun, J. X.; Lv, C. D. Template-based engineering of carbon-doped Co_3O_4 hollow nanofibers as anode materials for lithium-ion batteries. *Adv. Funct. Mater.* **2016**, *26*, 1428–1436.

[14] Liu, M. T.; Deng, X.; Ma, Y. D.; Xie, W. H.; Hou, X. Y.; Fu, Y. J.; He, D. Y. Well-designed hierarchical Co_3O_4 Architecture as a long-life and ultrahigh rate capacity anode for advanced lithium-ion batteries. *Adv. Mater. Interfaces* **2017**, *4*, 1700553.

[15] Huang, Y.; Fang, Y. J.; Lu, X. F.; Luan, D. Y.; Lou, X. W. Co_3O_4 hollow nanoparticles embedded in mesoporous walls of carbon nanoboxes for efficient lithium storage. *Angew. Chem., Int. Ed.* **2020**, *59*, 19914–19918.

[16] Zhang, K.; Xiong, F. Y.; Zhou, J. P.; Mai, L. Q.; Zhang, L. N. Universal construction of ultrafine metal oxides coupled in N-enriched 3D carbon nanofibers for high-performance lithium/sodium storage. *Nano Energy* **2020**, *67*, 104222.

[17] Sun, B. Y.; Lou, S. F.; Zheng, W.; Qian, Z. Y.; Cui, C.; Zuo, P. J.; Du, C. Y.; Xie, J. Y.; Wang, J. J.; Yin, G. P. Synergistic engineering of defects and architecture in Co_3O_4@C nanosheets toward Li/Na ion batteries with enhanced pseudocapacitances. *Nano Energy* **2020**, *78*, 105366.

[18] Cao, Z. Q.; Fu, J. M.; Wu, M. Z.; Hua, T.; Hu, H. B. Synchronously manipulating Zn^{2+} transfer and hydrogen/oxygen evolution kinetics in MXene host electrodes toward symmetric Zn-ions micro-supercapacitor with enhanced areal energy density. *Energy Storage Mater.* **2021**, *40*, 10–21.

[19] Yu, M. K.; Sun, Y. X.; Du, H. R.; Wang, C.; Li, W.; Dong, R. H.; Sun, H. X.; Geng, B. Y. Hollow porous carbon spheres doped with a low content of Co_3O_4 as anode materials for high performance lithium-ion batteries. *Electrochim. Acta* **2019**, *317*, 562–569.

[20] Sennu, P.; Madhavi, S.; Aravindan, V.; Lee, Y. S. Co_3O_4 nanosheets as battery-type electrode for high-energy Li-ion capacitors: A sustained Li-storage via conversion pathway. *ACS Nano* **2020**, *14*, 10648–10654.

[21] Lee, J. S.; Jo, M. S.; Saroha, R.; Jung, D. S.; Seon, Y. H.; Lee, J. S.; Kang, Y. C.; Kang, D. W.; Cho, J. S. Hierarchically well-developed porous graphene nanofibers comprising N-doped graphitic C-coated cobalt oxide hollow nanospheres as anodes for high-rate Li-ion batteries. *Small* **2020**, *16*, 2002213.

[22] Fan, H. Y.; Yi, G. Y.; Tian, Q. M.; Zhang, X. X.; Xing, B. L.; Zhang, C. X.; Chen, L. J.; Zhang, Y. L. Hydrothermal-template synthesis and electrochemical properties of Co_3O_4/nitrogen-doped hemisphere-porous graphene composites with 3D heterogeneous structure. *RSC Adv.* **2020**, *10*, 36794–36805.

[23] Kuai, L.; Geng, J.; Chen, C. Y.; Kan, E. J.; Liu, Y. D.; Wang, Q.; Geng, B. Y. A reliable aerosol-spray-assisted approach to produce and optimize amorphous metal oxide catalysts for electrochemical water splitting. *Angew. Chem., Int. Ed.* **2014**, *53*, 7547–7551.

[24] Cai, G. R.; Zhang, W.; Jiao, L.; Yu, S. H.; Jiang, H. L. Template-directed growth of well-aligned MOF arrays and derived self-supporting electrodes for water splitting. *Chem* **2017**, *2*, 791–802.

[25] Chai, Y. J.; Du, Y. H.; Li, L.; Wang, N. Dual metal oxides interconnected by carbon nanotubes for high-capacity Li- and Na-ion batteries. *Nanotechnology* **2020**, *31*, 215402.

[26] Zhang, Y. F.; Xie, M. H.; He, Y. B.; Zhang, Y. M.; Liu, L. D.; Hao, T. Q.; Ma, Y.; Shi, Y. F.; Sun, Z. J.; Liu, N. et al. Hybrid NiO/Co_3O_4 nanoflowers as high-performance anode materials for lithium-ion batteries. *Chem. Eng. J.* **2021**, *420*, 130469.

[27] Huang, S. J.; Yang, L. W.; Xu, G. B.; Wei, T. Y.; Tian, J.; Liu, X.; Li, H. P.; Xiang, Z. Y.; Cao, J. X.; Wei, X. L. Hollow Co_3O_4@N-doped carbon nanocrystals anchored on carbon nanotubes for freestanding anode with superior Li/Na storage performance. *Chem. Eng. J.* **2021**, *415*, 128861.

[28] Sun, H. X.; Du, H. R.; Yu, M. K.; Huang, K. F.; Yu, N.; Geng, B. Y. Vesicular $Li_3V_2(PO_4)_3$/C hollow mesoporous microspheres as an efficient cathode material for lithium-ion batteries. *Nano Res.* **2019**, *12*, 1937–1942.

[29] Liu, Y.; Peng, Y. M.; Naschitzki, M.; Gewinner, S.; Schöllkopf, W.; Kuhlenbeck, H.; Pentcheva, R.; Roldan Cuenya, B. Surface oxygen vacancies on reduced Co_3O_4(100): Superoxide formation and ultra-low-temperature CO oxidation. *Angew. Chem., Int. Ed.* **2021**, *60*, 16514–16520.

[30] Quast, T.; Aiyappa, H. B.; Saddeler, S.; Wilde, P.; Chen, Y. T.; Schulz, S.; Schuhmann, W. Single-entity electrocatalysis of individual “picked-and-dropped” Co_3O_4 nanoparticles on the tip of a carbon nanoelectrode. *Angew. Chem., Int. Ed.* **2021**, *60*, 3576–3580.

[31] Xu, K. Q.; Shen, X. P.; Song, C. S.; Chen, H. Y.; Chen, Y.; Ji, Z. Y.; Yuan, A. H.; Yang, X. L.; Kong, L. R. Construction of rGO-encapsulated Co_3O_4-$CoFe_2O_4$ composites with a double-buffer structure for high-performance lithium storage. *Small* **2021**, *17*, 2101080.

[32] Fang, L. B.; Bahlawane, N.; Sun, W. P.; Pan, H. G.; Xu, B. B.; Yan, M.; Jiang, Y. Z. Conversion-alloying anode materials for sodium ion batteries. *Small* **2021**, *17*, 2101137.

[33] Sun, R.; Bai, Y.; Luo, M.; Qu, M. X.; Wang, Z. H.; Sun, W.; Sun, K. N. Enhancing polysulfide confinement and electrochemical kinetics by amorphous cobalt phosphide for highly efficient lithium-sulfur batteries. *ACS Nano* **2021**, *15*, 739–750.

[34] Park, G. D.; Park, J. S.; Kim, J. K.; Kang, Y. C. Recent advances in heterostructured anode materials with multiple anions for advanced alkali-ion batteries. *Adv. Energy Mater.* **2021**, *11*, 2003058.

[35] Lu, J. L.; Li, J.; Wan, J.; Han, X. Y.; Ji, P. Y.; Luo, S.; Gu, M. X.; Wei, D. P.; Hu, C. G. A facile strategy of *in-situ* anchoring of Co_3O_4 on N doped carbon cloth for an ultrahigh electrochemical performance. *Nano Res.* **2021**, *14*, 2410–2417.

[36] Yao, Q. Q.; Gan, Y. M.; Ma, Z. J.; Qian, X. Y.; Cai, S. Z.; Zhao, Y.; Guan, L. H.; Huang, W. Approaching superior potassium storage of carbonaceous anode through a combined strategy of carbon hybridization and sulfur doping. *Energy Environ. Mater.* **2021**.

[37] Lim, K. R. G.; Handoko, A. D.; Nemani, S. K.; Wyatt, B.; Jiang, H. Y.; Tang, J. W.; Anasori, B.; Seh, Z. W. Rational design of two-dimensional transition metal carbide/nitride (MXene) hybrids and nanocomposites for catalytic energy storage and conversion. *ACS Nano* **2020**, *14*, 10834–10864.

[38] Huang, R. L.; Lin, J.; Zhou, J. H.; Fan, E. S.; Zhang, X. X.; Chen, R. J.; Wu, F.; Li, L. Hierarchical triple-shelled $MnCo_2O_4$ hollow microspheres as high-performance anode materials for potassium-ion batteries. *Small* **2021**, *17*, 2007597.

[39] Meng, T.; Li, B.; Wang, Q. S.; Hao, J. N.; Huang, B. B.; Gu, F. L.; Xu, H. M.; Liu, P.; Tong, Y. X. Large-scale electric-field confined silicon with optimized charge-transfer kinetics and structural stability for high-rate lithium-ion batteries. *ACS Nano* **2020**, *14*, 7066–7076.

[40] Shi, J. W.; Zu, L. H.; Gao, H. Y.; Hu, G. X.; Zhang, Q. Silicon-based self-assemblies for high volumetric capacity Li-ion batteries via effective stress management. *Adv. Funct. Mater.* **2020**, *30*, 2002980.

[41] Zhang, S. L.; Guan, B. Y.; Wu, H. B.; Lou, X. W. D. Metal-organic framework-assisted synthesis of compact Fe_2O_3 nanotubes in Co_3O_4 host with enhanced lithium storage properties. *Nano-Micro Lett.* **2018**, *10*, 44.

[42] Zhu, J. K.; Tu, W. M.; Pan, H. F.; Zhang, H.; Liu, B.; Cheng, Y. P.; Deng, Z.; Zhang, H. N. Self-templating synthesis of Hollow Co_3O_4 nanoparticles embedded in N,S-dual-doped reduced graphene oxide for lithium ion batteries. *ACS Nano* **2020**, *14*, 5780–5787.

[43] Zhang, R. H.; Li, Y.; Wang, M.; Li, D. W.; Zhou, J. J.; Xie, L.; Wang, T.; Tian, W.; Zhai, Y. J.; Gong, H. Y. et al. Super-assembled hierarchical CoO nanosheets-Cu foam composites as multi-level

hosts for high-performance lithium metal anodes. *Small* **2021**, *17*, 2101301.

[44] Du, H. R.; Huang, K. F.; Li, M.; Xia, Y. Y.; Sun, Y. X.; Yu, M. K.; Geng, B. Y. Gas template-assisted spray pyrolysis: A facile strategy to produce porous hollow Co_3O_4 with tunable porosity for high-performance lithium-ion battery anode materials. *Nano Res.* **2018**, *11*, 1490–1499.

[45] Adekoya, D.; Chen, H.; Hoh, H. Y.; Gould, T.; Balogun, M. S. J. T.; Lai, C.; Zhao, H. J.; Zhang, S. Q. Hierarchical Co_3O_4@N-doped carbon composite as an advanced anode material for ultrastable potassium storage. *ACS Nano* **2020**, *14*, 5027–5035.

[46] Liu, H. X.; Zhang, W. L.; Song, Y.; Li, L. L.; Zhang, C. W.; Wang, G. K. Superior rate mesoporous carbon sphere array composite via intercalation and conversion coupling mechanisms for potassium-ion capacitors. *Adv. Funct. Mater.* **2021**, *31*, 2107728.